

Design of Mixed-Cation Tri-Layered Pb-Free Halide Perovskites for Optoelectronic Applications

Zhun Liu, Xingang Zhao, Alex Zunger,* and Lijun Zhang*

To eliminate the toxic Pb^{2+} cation in hybrid halide perovskites, M^{3+} cations of Bi/Sb-based layered halide perovskites are being increasingly investigated for optoelectronic applications. However, such M^{3+} trivalent cations constrain the face-sharing bioctahedral or the bi-layered perovskites required to meet the charge neutrality condition. This usually gives rise to oversized indirect bandgaps and inferior carrier transport. Recent experiment suggested a mixed-cation tri-layered halide perovskite can be obtained by sandwiching a $[\text{Cu}^{2+}\text{X}_6]^{4-}$ layer between Sb^{3+} perovskite bilayers along the polar $[111]$ planes with cation ordering. A material design of mixed-cation $\langle 111 \rangle$ -oriented tri-layered Pb-free halide perovskite $\text{A}_4\text{MM}'_2\text{X}_{12}$ is studied by a computational screening of various combinations of M^{2+} cations (e.g., Zn^{2+} , Sn^{2+}) and M^{3+} cations (e.g., Bi^{3+} , Sb^{3+}). The thermodynamic stability of the candidate materials is systemically evaluated with respect to potential decomposition pathways and a series of stable compounds is synthesized. These results further indicate the chemical trend of electronic structure and how octahedral tilting coupling with charge ordering affects electronic properties. A protocol for engineering $\text{A}_4\text{MM}'_2\text{X}_{12}$ perovskites with optimized structures and electronic properties by exploiting octahedral tilting coupling with charge ordering in the polar $\langle 111 \rangle$ layered perovskites is established.

1. Introduction

Halide perovskites with general formula AMX_3 (A is monovalent alkali or organic cation, M is divalent group IV metalloid Pb^{2+} or Sn^{2+} , and X represents halide anion Cl^- , Br^- , or I^-) have attracted enormous attention for various optoelectronic applications over the last few years owing to their flexibly tunable bandgap, high efficient photoluminescence yield, narrow emission line width, as well as superior charge carrier transport properties.^[1–4] Taking solar cell as an instance, hitherto,

the recorded photovoltaic (PV) efficiency is over 23% in the laboratory.^[1,4–6] Such merits for high-performance optoelectronics are governed by their unique electronic structure features, which can mainly be attributed to the ns^2 lone-pair electrons of Pb^{2+} and Sn^{2+} cations.^[7,8] The presence of ns^2 cations in these perovskites gives rise to pronounced curvature in both valence and conduction band edges through considerable anti-bonding hybridization with the halide anions. This facilitates the formation of the shallow defect states to induce carriers, balanced and low electron and hole effective masses for efficient charge transport and carrier extraction.^[8,9] Additionally, the enhanced Born effective charges (relative to nominal ionic charges) and large static dielectric constant contribute to screening charged defects and impurities, thereby suppressing carrier scattering and trapping.^[7,10] Despite the progress achieved in halide perovskites for optoelectronic applications, the poor long-term material and device stability under normal

operation condition impedes their commercialization,^[4,11,12] though protecting active perovskite layers,^[4,6,9] mixing organic and inorganic A site ions,^[13,14] and exploiting low-dimensional counterparts have shown enhanced stability.^[14–16] More importantly, at this stage it is not clear whether the toxic issue of Pb^{2+} ions would hinder the practical device application of halide perovskites.

In this regard, eco-friendly Bi^{3+} - and Sb^{3+} -based perovskites with the similar ns^2 electron configuration as Pb^{2+} have attracted significant research interest.^[17–19] Within the three-dimensional (3D) perovskite framework formed by corner-sharing octahedral motifs, lead-free double halide perovskites have been proposed by hetero-substituting Pb^{2+} with the cation pair of monovalent metal (e.g., Na^+ , Ag^+) and trivalent metal (e.g., Sb^{3+} , Bi^{3+} , and In^{3+}) by exploiting the cation transmutation principle in conventional tetrahedral semiconductors.^[20–23] It is worth noting that the predicted inorganic double perovskites, such as $\text{Cs}_2\text{AgBiCl}_6$, $\text{Cs}_2\text{AgBiBr}_6$, $\text{Cs}_2\text{AgInCl}_6$, have been experimentally proved more stable against decomposition under humidity and light emission.^[21,22,24] However, these quaternary double perovskites exhibit weak light emission/absorption because of the indirect bandgap feature or the parity-forbidden band-edge transition.^[21,24,25] While for the purely Sb^{3+} - and Bi^{3+} -based perovskites, they show enhanced air-stability but

Dr. Z. Liu, Dr. X. Zhao, Prof. L. Zhang
 State Key Laboratory of Superhard Materials
 Key Laboratory of Automobile Materials of MOE
 and School of Materials Science and Engineering
 Jilin University
 Changchun 130012, China

E-mail: lijun_zhang@jlu.edu.cn

Dr. X. Zhao, Prof. A. Zunger
 University of Colorado and Renewable and Sustainable Energy Institute
 Boulder, Colorado 80309, USA
 E-mail: Alex.Zunger@colorado.edu

 The ORCID identification number(s) for the author(s) of this article can be found under <https://doi.org/10.1002/aelm.201900234>.

DOI: 10.1002/aelm.201900234

the charge neutrality condition constrains the ability to form a 3D corner-sharing perovskites structure.^[17,18,26] Instead, it forms compounds with 0D isolated dimer structure (with face-fused bi-octahedron) or 2D layered structure (with corner-sharing octahedron).^[17,18,26,27] Generally, the low-dimensional derived M^{3+} halide makes a framework with the unit formula of $A_{n+1}M_nX_{3n+3}$ being stabilized by stoichiometric cationic sublattices and slices along the [111] planes from the bulk phase.^[26,28] As a consequence, it has limited to form M^{3+} bilayer $A_3M_2X_9$ ($n = 2$) due to the fractional averaged valence state of $2 + 2/n$ for M cation. Further developing these quasi-2D Sb-/Bi-based derivate halide perovskites requires mixed valence of cations in a structural formula of $A_{n+1}M_{n-2}M'X_{3n+3}$ to resolve above charge balance requirements.^[1,29]

A recent study on tri-layered mixed-cation halide perovskite provides a feasible demonstration of the above strategy by sandwiching a single $[MX_6]^{4-}$ layer with $M^{2+} = Cu^{2+}$ between the $\langle 111 \rangle$ -layered $A_3M'_2X_9$ phase perovskite (with $M'^{3+} = Sb^{3+}$, C2/M structure in **Figure 1a**).^[30] Compared with the bilayer $A_3M'_2X_9$ phase perovskite with wide bandgaps in the range of 1.89–2.06 eV, the $Cs_4CuSb_2Cl_{12}$ exhibits a direct bandgap of 1.0 eV and excellent photo and thermal stability, thus intriguing further exploration of tri-layered perovskites by equivalent substitution of $2+$ cations. In principle, the target cation replacement of Cu^{2+} should be stable and have good orbital overlap

with the $[SbCl_6]^{3-}$ octahedrons.^[31] Tang et al., thus, have taken first-principles calculation to study the quasi-2D Sb^{3+} -based derivate halide perovskites of $Cs_{3+n}M(II)_nSb_2X_{9+3n}$ ($M = Sn^{2+}$, Ge^{2+}) system using n -layer $Cs(Sn/Ge)I_3$ artificially inserted to the $Cs_3Sb_2I_9$.^[29] In the same way, Huang and co-workers have further searched the new series of $A_4MM'_2X_{12}$ compounds with $A = Cs^+$, $M =$ group IIA ($Mg^{2+}/Ca^{2+}/Sr^{2+}$)/group IIB (Zn^{2+}/Cd^{2+})/group IVA (Sn^{2+}), $M'^{3+} = Sb^{3+}/In^{3+}/Bi^{3+}$, and XVII = $Cl^-/Br^-/I^-$ as used for p-type transparent conductors.^[32] However, both of these studies directly use the structural skeleton (C2/M) proposed experimentally for $Cs_4CuSb_2Cl_{12}$ and choose limited reaction pathways to evaluate the stability of a hypothetical compound.^[29,32] This would beg the questions whether the adopted C2/M skeleton is the lowest ground-state phase, and the stability analysis of a given compound with respect to a few selective decomposition pathways completely reflects the realistic experimental condition.

Apart from those proofs for prediction of the new layered halide crystals, another critical issue concerns the perovskites undergoing structural phase transitions associated with octahedral tilting.^[33,34] Along with the changes of the lattice parameters, the phase transition was associated with the in-phase or out-of-phase tilting of the octahedron in consecutive layers. These layered $A_4MM'_2X_{12}$ perovskites are B-site vacancy ordering structures which can be treated as a subgroup of the

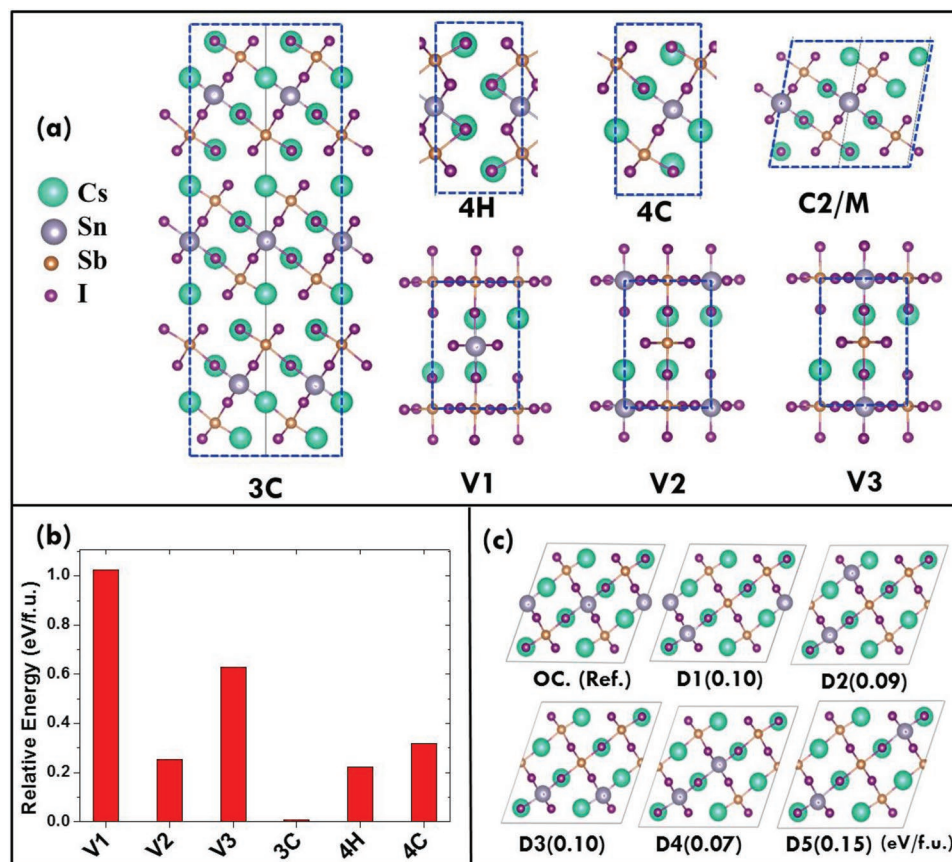


Figure 1. a) Hypothetical skeleton structures for $A_4MM'_2X_{12}$ perovskites. b) The relative energy of hypothetical skeleton structures in comparison to the C2/M crystal structure. c) Relative energies of possible M^{2+}/M^{3+} cations interdiffusion configurations (D1–D5) versus the ordered cations (OC) in $Cs_4SnSb_2I_{12}$ perovskites. The C2/M unit cell contains two formal units and the lowest energy configuration is set to zero as the reference structure.

parent ABX_3 perovskites.^[35] However, it involves more complexity due to the layered charge order and its discontinuity along the [111] direction. In comparison with the tilting equivalents in the parent cubic symmetry groups, the B-site cation order along the [111] direction makes the R_4^+ octahedral tilting to distinguishing between a positive ($a^-a^-c^0$) and a negative rotation ($-a^-a^-c^0$) along the [110] direction.^[35] These different type of distortion correlates with the redistribution of the ion charge and bonding angles, which affect the electronic properties and structural stability.^[33,36–38] Thus, the mixed-cation in the layered perovskite provides a living example to explore the coupling between the structural charge order and the octahedral tilting preferences in $A_4MM'_2X_{12}$ structure prototype.

Here we take a systematic screening procedure to explore the stability and optoelectronic property of the candidate $A_4MM'_2X_{12}$ compounds. Based on the above discussion, the Sn^{2+} and Zn^{2+} are intuitively the preferable cations due to their nearby element position with Sb^{3+} and Cu^{2+} in the periodic table, respectively. We, thus, extend precise screening steps and filters to study the possible ion combinations in $A_4MM'_2X_{12}$ halide compound with different cations for A = (K^+ and Cs^+), M = (Zn^{2+} and Sn^{2+}), M' = (Bi^{3+} and Sb^{3+}), and three types of ions for X = (Cl^- , Br^- , and I^-). First, we have taken two steps to determine the ground-state structural scaffold and atomic configuration. Second, two filters (simple decomposition pathways and triangle phase diagram analysis) are taken to determine the thermodynamic stability of the compounds with respect to the competing phases. Considering the Rb^+ with radius in-between the Cs^+ and K^+ , we have the preliminary screening of the potential stable $A_4MM'_2X_{12}$ compounds in 24 combinations for two types of ions (i.e., K^+ and Cs^+) on A site, then examine the qualified compounds for Rb-based $A_4MM'_2X_{12}$ by analogy. After the stability screening steps, the optoelectronic properties of the qualified compounds are explored. We further identify the physical origin of tilting preference in the $A_4MM'_2X_{12}$ perovskites. The tilting modes correlated to the indirect-to-direct bandgap transitions are finally discussed.

2. Computational Methods

First-principles calculations were performed on the basis of density functional theory (DFT) methods using the projector-augmented wave (PAW) method, as implemented in the Vienna ab initio simulation package (VASP).^[39,40] We described the long-range van der Waals interaction for the layered halide perovskites as implemented in the optimized exchange van der Waals functional B86b of Becke (optB86b-vdW).^[41] The atomic positions were optimized using the conjugate gradient scheme until the maximum force on each atom was less than $0.02 \text{ eV } \text{Å}^{-1}$.^[42] The electronic structures and other related properties were carefully tested to be converged with an energy cutoff of 520 eV for the plane wave basis and a k-spacing of 0.125 Å^{-1} for the sampling of the Brillouin zone. The band structure calculations were compared with the effect of spin-orbit coupling (SOC) as well as the Heyd–Scuseria–Ernzerhof (HSE06) hybrid functional.^[43] The optical absorption spectra, the SOC effect, and the HSE bandgap corrections were taken

into account to remedy the absorption spectra edges and the optical gaps. The effective masses were calculated by

$$M_{\beta u}^{-1}(i, k) = \frac{1}{\hbar^2} \frac{\partial^2 \epsilon_{i,k}}{\partial k_\beta \partial k_u} \quad (1)$$

as implemented in BoltzTraP code, which solves the Boltzmann equation by a smoothed Fourier interpolating of bands.^[44] The electronic structures and other related properties were carefully tested to be converged with an energy cutoff of 520 eV for the plane wave basis and a k-spacing of 0.125 Å^{-1} for the sampling of the Brillouin zone. More detailed validation of the computational approaches for the halide perovskite materials has been indicated in our previous comprehensive materials screening studies.^[20,23,45] We also have tested the layered perovskite (e.g., $P\bar{3}m1$ $Rb_3Sb_2Br_9$) with optimized lattice parameters ($a = 7.741 \text{ Å}$, $c = 9.635 \text{ Å}$), PBE bandgap (1.76 eV), and HSE06 bandgap (2.35 eV), which are in good agreement with the experimental values ($a = 7.848 \text{ Å}$, $c = 9.612 \text{ Å}$, and 2.48 eV).^[17]

3. Results and Discussion

3.1. Thermodynamic Selection Filters for the Rational Design of Tri-Layered Halide Perovskites

We illustrate the principles of constructing a set of thermodynamic filters that were applied to the tri-layer halide perovskites.

3.1.1. Selection of Ground State Scaffold Structure for $A_4MM'_2X_{12}$

To figure out the lowest-energy scaffold for $A_4MM'_2X_{12}$ as shown in Figure 1a, we used four types of halide structures: two types of structures were found in the Inorganic crystal structure database (ICSD),^[46,47] i.e., $K_4Fe(II)Fe(III)_2F_{12}$, (3C) and $Cs_4PdMn_2F_{12}$, (V1-3), the third type is the experimentally synthesized $Cs_4CuSb_2Cl_{12}$ (C2/M), and the fourth type is derived structure from $Cs_3Sb_2I_9$ (4H/4C). Considering the different atomic occupation and stacking periodicity, we have compared the total energy for $Cs_4SnSb_2I_{12}$ in 7 derivative structures. Figure 1b clearly indicates that other 6 hypothetical skeletons are relatively higher than the C2/M structure. Especially, the vacancy ordered structures (from the $Cs_4PdMn_2F_{12}$ structural prototype) show much higher energy (at least $0.25 \text{ eV f.u.}^{-1}$) than the C2/M structure. It should be noted that the 3C structure (from the $K_4Fe_3F_{12}$ crystal) has nearly equal energy as the C2/M crystal due to the almost identical chemical coordination between them. The 4C crystal is one-third of the 3C structure along the z-direction and only exhibits different interlayer octahedral stacking and sliding periodicity. As a consequence, the 4H and 4C structures are 0.22 and 0.32 eV f.u.^{-1} higher than the C2/M, implying the unfavorable interlayer stacking between the octahedral layers in those structures. Therefore, we finally choose the C2/M scaffold for $A_4MM'_2X_{12}$ in the subsequent study.

We further examined the relative energy of cation interdiffusion configurations (M^{2+}/M^{3+}) versus the cation ordered structure with a sandwiched Sn^{2+} layer. As shown in Figure 1c, the

relative energy in the other 5 Sn–Sb exchanged configuration (D1–D5) is at least 0.07 eV f.u.⁻¹ higher than the reference structure (OC). Thus, we choose the tri-layered cation ordered perovskite as the tentative structure for A₄MM′₂X₁₂. After the structure optimization, we find that all of the K-based perovskites only adopt octahedral tilting configurations (*a*⁻*b*⁻*c*⁰ in Glazer’s notation) while the Cs-based structures can adopt both original flat (*a*⁰*b*⁰*c*⁰) and slightly tilting (*a*⁻*b*⁻*c*⁰) structures. The total energies in those tilting configurations are lower energy than the flat layered structures. Thus, we take the tilting octahedron (*a*⁻*b*⁻*c*⁰) configuration in further thermodynamic stability analysis.

3.1.2. Thermodynamically Stabilities Analysis

After establishing the ground-state structure for the compounds in step A, we next enquire which decorations are stable with respect to the decomposition to competing phases. For efficient screening of stable materials, we have used the two filters in step B. In step B.1, we considered 3 simplified decomposition pathways, then in step B.2, we considered all possible competing pathways through triangle analysis.

B.1 Simplified Decomposition Trends for the Thermodynamic Stability: In step B.1, we have considered three decomposition pathways:

- Decompose into binaries halides: A₄MM′₂X₁₂ → 4AX + MX₂ + 2M′X₃ (red bars);
- Decompose into binaries and ternary dimer A₃M′₂X₉: A₄MM′₂X₁₂ → AX + MX₂ + A₃M′₂X₉ (blue bars);
- Decompose into binaries and ternary layered A₃M′₂X₉: A₄MM′₂X₁₂ → AX + MX₂ + A₃M′₂X₉-L (green bars).

The comparisons of decomposition pathways can give a quantitative stability tendency for the A₄MM′₂X₁₂ and the A₃M′₂X₉ compounds and then help us to exclude the unstable

candidates. When the A₃M′₂X₉ structures do not exist in ICSD, the relevant hypothetical dimer and layered phases are constructed by replacing the target elements from the Cs₃Sb₂I₉ structural prototypes (both dimer and layered have reported) and then relax them to the local energy minima. The positive decomposition enthalpy, for example, Δ*H* (A₄MM′₂X₁₂) = *E*(AX) + *E*(MX₂) + *E*(A₃M′₂X₉) – *E*(A₄MM′₂X₁₂), means the compound is stable with respect to corresponding decomposition pathway (b). As depicted in Figure 2, we can separate the compounds into the following four categories by the stability character:

- The red bars are lower energy than the blue and green ones but all of them have positive values, e.g., K₄SnSb₂Cl₁₂, K₄SnSb₂Br₁₂, K₄SnBi₂Br₁₂, K₄ZnSb₂Cl₁₂, and K₄ZnSb₂Br₁₂. These 5 compounds have positive decomposition enthalpy for all pathways and all of them are more stable than the ternary dimer or layered K₃M′₂X₉ phase, which also indicates that the hypothetical competing A₃M′₂X₉ phase is unstable. Therefore, more stable ternary competing phases should further take into consideration.
- The red bars have negative values and lower than the blue and green bars, e.g., K₄SnSb₂I₁₂, K₄SnBi₂I₁₂, K₄ZnSb₂I₁₂, K₄ZnBi₂Br₁₂, and K₄ZnBi₂I₁₂. The negative enthalpy indicates that these K-based compounds (especially for the iodine compounds) are unstable. This is also reasonable that small cation of K⁺ is incompatible to the large I⁻ ionic frameworks. Thus, we exclude these compounds at this step.
- The red bars are higher than the blue and green bars and all of them have positive values, e.g., K₄SnBi₂Cl₁₂, K₄ZnBi₂Cl₁₂, Cs₄SnSb₂Cl₁₂, Cs₄SnSb₂I₁₂, Cs₄SnSb₂Br₁₂, Cs₄SnBi₂Cl₁₂, and Cs₄SnBi₂Br₁₂. These 7 compounds are stable against the above three pathways, but the A₃M′₂X₉ phases are also stable compounds. Therefore, these compounds still need to analyze more competing pathways.
- The blue or green bars have negative values, e.g., Cs₄SnBi₂I₁₂, Cs₄ZnSb₂Cl₁₂, Cs₄ZnSb₂Br₁₂, Cs₄ZnSb₂I₁₂,

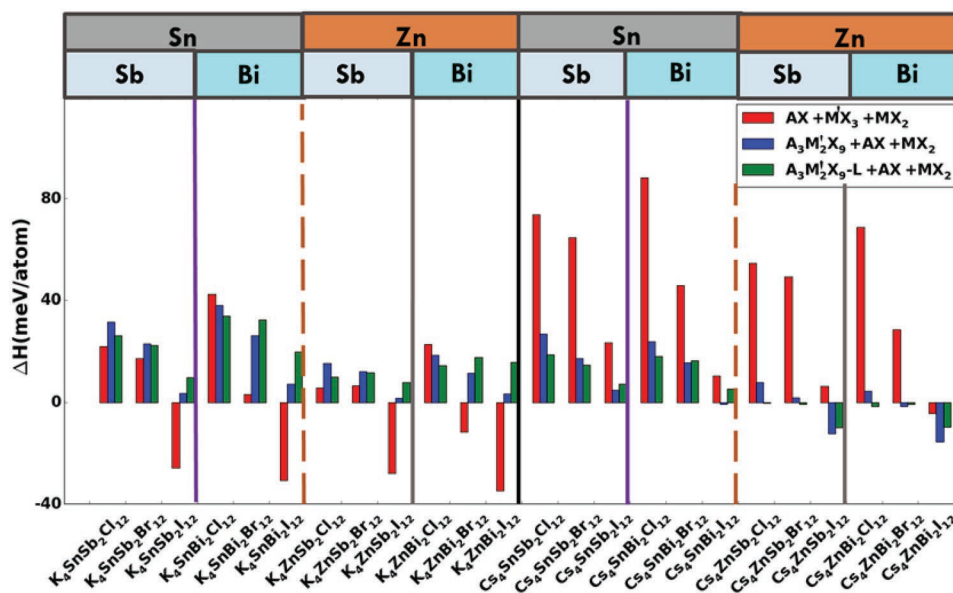


Figure 2. Decomposition enthalpies of A₄MM′₂X₁₂ with respect to 3 simple decomposition pathways. The red, blue, and green bars represent the decomposition reactions along the (a), (b), and (c) pathways, respectively.

Cs₄ZnBi₂Cl₁₂, Cs₄ZnBi₂Br₁₂, and Cs₄ZnBi₂I₁₂. These compounds can be excluded because they are unstable against the A₃M'X₉ phase compounds.

The tendency of the enthalpies in Figure 2 shows that the stability for all combinations are decreasing when the halide ions changing from Cl, Br to I. These chemical trends are in agreement with other halide perovskites due to the decreasing ionic bonding strength.^[48] We can see that K- and Cs-based chlorides and bromides (i.e., A₄SnSb₂X₁₂, A₄SnBi₂X₁₂, A₄ZnSb₂X₁₂, A₄ZnBi₂X₁₂, A = K⁺, Cs⁺, X = Cl⁻, Br⁻) have positive or near to zero decomposition enthalpies with respect to (a–c) decomposition pathways. It implies that these K- and Cs-based chlorides and bromides are stable with respect to these three decomposition pathways. While for the K-based iodides, all of them are unstable due to the large negative decomposition enthalpy against its binary halide compounds. There still remain 12 stable compounds (including 6 chlorides: K₄SnSb₂Cl₁₂, K₄SnBi₂Cl₁₂, K₄ZnSb₂Cl₁₂, K₄ZnBi₂Cl₁₂, Cs₄SnSb₂Cl₁₂, and Cs₄SnBi₂Cl₁₂; 5 bromides: K₄SnSb₂Br₁₂, K₄SnBi₂Br₁₂, K₄ZnSb₂Br₁₂, Cs₄SnSb₂Br₁₂, and Cs₄SnBi₂Br₁₂, and 1 iodide: Cs₄SnSb₂I₁₂) with positive Δ*H* refer to above three decomposition pathways (a–c). In the next section, we employ the triangle analysis (i.e., considering more competing phases) to determine the thermodynamic stabilities of the selected 12 candidates.

B.2 Triangle Analysis with More Competing Phases: Under the thermodynamic equilibrium conditions, the chemical potential of each element in a thermodynamic stable hypothetical compound should be lower than it to form any possible competing phases.^[49] Thus, to rule out all possible competing decomposition channels, the following equality and a set of inequalities need to be satisfied simultaneously

$$\mu A_4MM'_2X_{12} = 4\mu A + 2\mu M' + \mu M + 12\mu X \quad (2)$$

$$\Delta\mu I = \mu I - \mu_0 \leq 0, I = A, M, M', X \quad (3)$$

$$4\Delta\mu A + 2\Delta\mu M' + \Delta\mu M + 12\Delta\mu X = \Delta H_f(A_4MM'_2X_{12}) \quad (4)$$

$$n(i)\Delta\mu A + m(i)\Delta\mu M + p(i)\Delta\mu M' + q(i)\Delta\mu X \leq \Delta H_f(A_{n(i)}M_{m(i)}M'_{p(i)}X_{q(i)}), i = 1, \dots, Z \quad (5)$$

where Δ*μ**I* is the chemical potential of element *I* vary from the standard phase of the element with zero-point energy as μ₀, Δ*H*_f is the formation enthalpy, and *n*(*i*), *m*(*i*), *p*(*i*), *q*(*i*), are the stoichiometries for each competing phase. Controlling the special potential bias, each competing phase cuts off a part of the plane in the reduced dimensional potential space. If a part of the chemical potential region is left after considering all competing phases, then this candidate compound should be stable against all possible decomposition channels under the thermodynamic equilibrium conditions.

To construct the competing phases for triangle analysis, we considered known elemental, binary, and ternary competing phases with the structures taken from the ICSD. Importantly, we have constructed the possible ternary competing phases (A₂M'X₅, A₃M'X₆, A₃M'X₉, A₂MX₆, AM₂X₅, and AMX₃, which

not included in the ICSD) by ionic transmutation with its isovalent compounds in ICSD to make sure that all candidate compounds can resist all possible competing phases.^[49,50] This extra filter using hypothetical ternary compounds to strengthen the screening of stability would help to avoid false positive predictions, though it would shrink the stability region. These presumed compounds may not emerge as the real competing phases during the growth with controlled chemical potential, but they can provide auxiliary evidence to the reliable prediction of new stable compounds.

We used these competing phases for phase stability analysis over 12 primary screened structures from step B.1. Considering the Rb⁺ have size in-between the Cs⁺ and K⁺ cations, we also examined the qualified compounds for Rb-based A₄MM'X₁₂ by analogy. After the phase diagram stability analysis, all of the Cs- and Zn-based compounds have excluded out and there remain six compounds containing a stable chemical potential region: K₄SnBi₂Cl₁₂, K₄SnSb₂Cl₁₂, K₄SnSb₂Br₁₂, Rb₄SnBi₂Cl₁₂, Rb₄SnSb₂Br₁₂, and Rb₄SnSb₂Cl₁₂. Therefore, these compounds may be synthesized under controllable conditions. The detailed phase diagrams for the qualified stable compounds (see in Figure S1, Supporting Information) and the example of main competing phase variation with controlled chemical potential (see in Figure S2, Supporting Information) are discussed in the Supporting Information.

3.2. Optoelectronic Properties of the Stable A₄MM'X₁₂ Perovskites

3.2.1. Electronic Structure

Before discussing the electronic properties of the screened new materials, we first examine the parameters computed for the well-known perovskite CsPbBr₃ as partial validation of the calculation method. In comparison to the experimentally reported gap value (2.25 eV), the calculated bandgaps by HSE functional, PBE functional, PBE+SOC, and HSE+SOC methods are 2.6, 1.96, 0.99, and 1.65 eV, respectively (see in Table 1 and Table S1, Supporting Information). It indicates that the standard PBE

Table 1. Calculated bandgaps and effective masses of the band edges for 6 stable A₄MM'X₁₂. The HSE corrections on the PBE+SOC approaches enlarge the bandgaps by 0.53–0.67 eV, see details for PBE functional and PBE+SOC calculated bandgaps in Table S1 in the Supporting Information. Note that the SOC effects can reduce the bandgap but give more accurate band edge.

	HSE+SOC Bandgap values [eV]		Effective mass at band edges [m ₀]	
	E _g ^d	E _g ^{ind}	m _e [*]	m _h [*]
CsPbBr ₃ ^{a)}	1.65[2.25]	–	0.79[0.23]	0.25[0.23]
K ₄ SnSb ₂ Cl ₁₂	2.67	2.63	0.95	0.95
K ₄ SnBi ₂ Cl ₁₂	2.59	2.54	0.81	1.71
K ₄ SnSb ₂ Br ₁₂	2.20	2.17	0.58	0.91
Rb ₄ SnSb ₂ Cl ₁₂	2.52	2.45	1.10	0.84
Rb ₄ SnBi ₂ Cl ₁₂	2.51	2.43	1.02	1.59
Rb ₄ SnSb ₂ Br ₁₂	2.10	2.07	0.68	0.84

^{a)}Comparison of our computed and other experimental measured parameters (in the brackets) for the reference compound CsPbBr₃.^[55]

functional predicated bandgaps are even more close to the real values. Typically, the standard PBE functional severely underestimates the bandgaps for most wide bandgap semiconductors due to its unphysical self-Coulomb repulsion.^[51] However, the spin-orbit coupling has a strong effect on the lead halide perovskites, reducing the bandgap by up to roughly 1.0 eV; thus these two effects have canceled each other in the standard PBE predictions.^[3,52] For the heavier homologous element, Bi, with its more relatively contracted s-like states, we expect similar bandgap reduction; thus, the PBE functional would give a closer prediction. While the SOC effect on other Sn- and Sb-based perovskites was found to be weaker. As discussed in the Computational Methods section, the 2D layered $\text{Rb}_3\text{Sb}_2\text{Br}_9$ has measured gap of 2.48 eV and the PBE calculated bandgap of 1.76 eV, while HSE06 functional gives a closer prediction (2.35 eV), which implies a reliable method in the community. To get accurate bandgap prediction for the new compounds, we take the hybrid functional to correct the bandgap obtained by using PBE function with the SOC effects. The results are illustrated in Table 1 and Figure 3. All 6 compounds have quasi-direct band edge transition from valence band maxima (VBM) at Z point to the conduction band minima (CBM) at G point because the energy difference between the direct and indirect bandgaps in these compounds is very small (0.02–0.12 eV). Therefore, the direct bandgap transitions for those compounds

are within the range of visible light region (2.1–2.7 eV). From Figure 3 and Table 1, we can clearly see that the gap values increase with reducing the cation size from $A = \text{Rb}^+$ to K^+ for $\text{A}_4\text{SnM}'_2\text{X}_{12}$. For example, $\text{Rb}_4\text{SnBi}_2\text{Cl}_{12}$ and $\text{Rb}_4\text{SnSb}_2\text{Br}_{12}$ with bandgaps of 1.86 and 1.57 eV have increased to 1.92 and 1.64 eV as for $\text{K}_4\text{SnBi}_2\text{Cl}_{12}$ and $\text{K}_4\text{SnSb}_2\text{Br}_{12}$, respectively. This is because the smaller K^+ cation induces larger bond angle distortions in the $[\text{SnX}_6]^{4-}$ octahedrons, which destabilizes the antibonding from X(s/p) hybridization with the Sn(5p) orbitals while stabilizes it with the Sn-s orbitals. Thus it elevates the conduction band edges and reduces the valence band edges.^[53,54] A similar chemical trend was observed in the halide ions, i.e., from Br^- to Cl^- , the bandgap increased from 1.57 eV in $\text{Rb}_4\text{SnSb}_2\text{Br}_{12}$ to 1.64 eV in $\text{Rb}_4\text{SnSb}_2\text{Cl}_{12}$. This bandgap reduction can be understood on the basis of decreasing the energy in X(p) orbitals from Br^- to Cl^- . The smaller ionic size and higher electronegative in Cl^- increase the ionic contribution in the hybrid orbital splitting, thus decreasing the valence bands and increasing the splitting of bandgaps.^[2,34,48]

3.2.2. The Carrier Effective Masses

The carrier effective masses contribute to their ambipolar conductivity and diffusion length. Thus, we calculated the effective

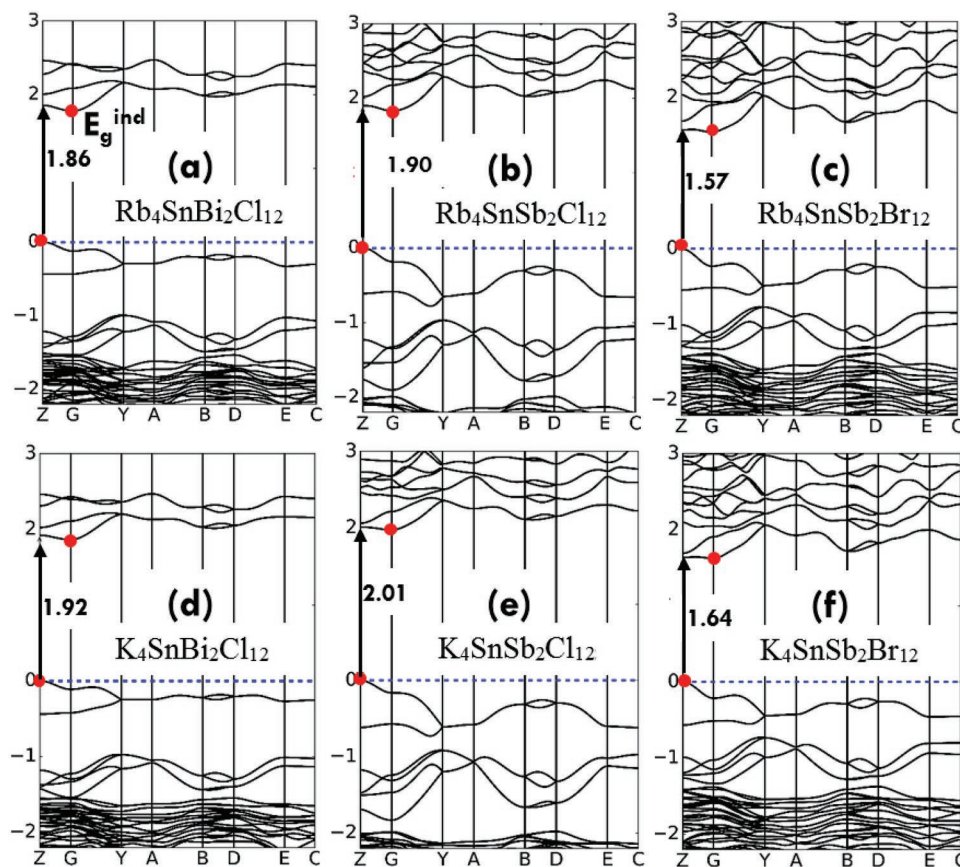


Figure 3. Calculated band structures with PBE functional including SOC effects. a–f) for $\text{Rb}_4\text{SnBi}_2\text{Cl}_{12}$, $\text{Rb}_4\text{SnSb}_2\text{Cl}_{12}$, $\text{Rb}_4\text{SnSb}_2\text{Br}_{12}$, $\text{K}_4\text{SnBi}_2\text{Cl}_{12}$, $\text{K}_4\text{SnSb}_2\text{Cl}_{12}$, and $\text{K}_4\text{SnSb}_2\text{Br}_{12}$, respectively. The minimal direct bandgap transition is indicated by the arrows and the CBM and VBM for the minimal indirect band transitions are indicated by the red dots. The indirect bandgap values E_g^{ind} are listed in the figures.

masses of electrons and holes for the 6 stable compounds and listed them in Table 1. The testified effective masses (m_e^* and m_h^*) of the carriers for CsPbBr₃ are 0.79 and 0.25 m_0 , which are slightly higher than the experimental measured 0.23 m_0 for both holes and electrons at room temperature.^[55] More often, the experimental measured physical parameters not only depend strongly on the crystal growth but also on other sample issues from the device fabrication.^[52,54,56] Thus, it is generally seen that the theoretic calculations can marginally deviate from the measured values. As shown in Table 1, the masses of holes in all Bi-based compounds are slightly heavier than the Sb-based compounds. This trend is in agreement with the weak coupling between the Bi(6s) and Sn(5s) orbitals, which results in narrow energy band dispersions at the valence band edges.^[17] Specifically, reducing the cation size from Rb⁺ to K⁺ makes the effective masses for electrons smaller while the holes become slightly heavier. This opposite carrier mass variation trend is in accord with the dispersion of band edges, which can be understood from the changing of hybridization between the orbital overlaps. For the larger bond angle distortions in K-based perovskites, the antibonding orbitals between X(p) with M(s) for the valence states are stabilized while the interactions with the M(p) orbitals for the conduction bands are destabilized, thereby reducing of band curvature in the valence edges but increasing it in the conduction band edges.^[3,53]

3.2.3. Optical Absorption Spectra

Figure 4 shows the calculated optical absorption spectra for the 6 stable A₄MM'X₁₂ by using PBE functional. It can be seen that these compounds exhibit strong absorption coefficient (above $5 \times 10^4 \text{ cm}^{-1}$) and steep absorption onset. A sharp absorption threshold is contributed by the dipole-allowed optical transitions with a high joint density of states (JDOS) near the band edges.^[57] From a qualitative viewpoint, the optical transitions from (Sn(s) + X(p)) to Sb/Bi(p) orbitals are dipole allowed and the relatively flat bands near the band edge guarantee a high JDOS, thereby resulting in an abrupt absorption onset.^[3,37,48]

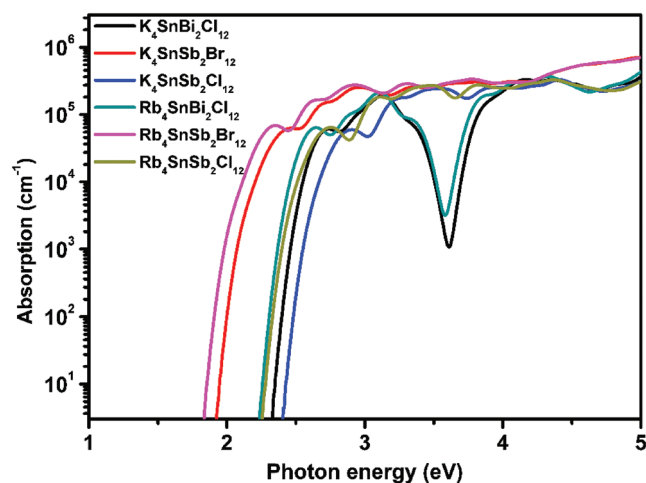


Figure 4. a) Calculated spectrum of the optical absorption of the 6 stable A₄MM'X₁₂ compounds.

Though these ns² electronic compounds with high absorption coefficients and rapid onsets, the absorption spectra for Rb₄SnBi₂Cl₁₂ and K₄SnBi₂Cl₁₂ exist a slight reduction in the energy range of 3.3–3.7 eV. It implies a relatively weak hybridization of the subvalence bands in these Bi-based perovskites.

3.2.4. Electronic States Decorated by Different Atomic Orbital Hybridization

The density of states (DOS) calculations can accurately reproduce the discrete orbital contributions. In general, strong hybridization-induced broadening electronic states in solids requires both spatial and energy overlap between their orbital wavefunctions.^[2,3,58] Cations mixing breaks the translational and energetically connectivity of wavefunction to form discrete bands.^[58] As depicted by the red rectangle in Figure 5a, the conduction and valence band edges split into two separated peaks due to the incompatible orbital overlap between the Sn and Bi. From the atomic projected DOS, the conduction band edges in K₄SnBi₂Cl₁₂ are dominated from the weak hybridization between Bi(6p) and Sn(5p) orbitals with Cl(3p), while the valence band edges are contributed by the separated Sn²⁺ (5s²) and Bi³⁺ (6s²). We further schematically depicted these orbital coupling between the metal cation and halide ion near the band edges in Figure 5b. While for the projected DOS in Rb₄SnSb₂Br₁₂ (see in Figure 5c,d), the band edges state exhibit more dispersive contributions from both Sb and Sn, which implies a broadening of the orbital overlap between their 5s and 5p orbitals. One possible interpretation for the weak hybridization in Bi-based compounds is attributed to the contraction of Bi 6s and 6p orbitals by the relativistic effects, thus reducing the reactivity of shell electrons in comparison to the Sb-based compounds.^[17] Thus, the Sb-based perovskites show more broad orbital interactions for the band edges (see in Figure 5c,d).

3.3. Origin of Octahedral Tilting Preference in A₄MM'X₁₂ Perovskites

The cubic ABX₃ perovskite structure is usually only observed at high temperature, while a group of lower symmetry phases emerges at lower temperatures.^[33] The associated new phases are driven by a range of symmetry breaking induced lattice tilting from the cubic phase.^[34,36] The relative stability of an inorganic halide perovskite tilting correlates with the volume decrease and the A-site displacement. For example, the prototypical halide perovskite CsSnBr₃ undergoes tilting phase transition sequence from high symmetry cubic α phase ($a^0a^0a^0$) to the low symmetry tetragonal β phase ($a^0a^0c^+$) and then to the orthorhombic γ phase ($a^-a^-c^+$) with gradually decreasing temperatures.^[36] As illustrated in Figure 6, two basic tilting modes induced phase transition accompanied octahedron rotation were denoted as M₃⁺ and R₄⁺. The former is associated with the in-phase tilting of the octahedron in successive layers where every octahedron along the axis rotates in the same direction by the same amplitude, while the latter is corresponding to the out of phase tilting where the rotation changes sign for each octahedron along the rotation axis.^[35,36]

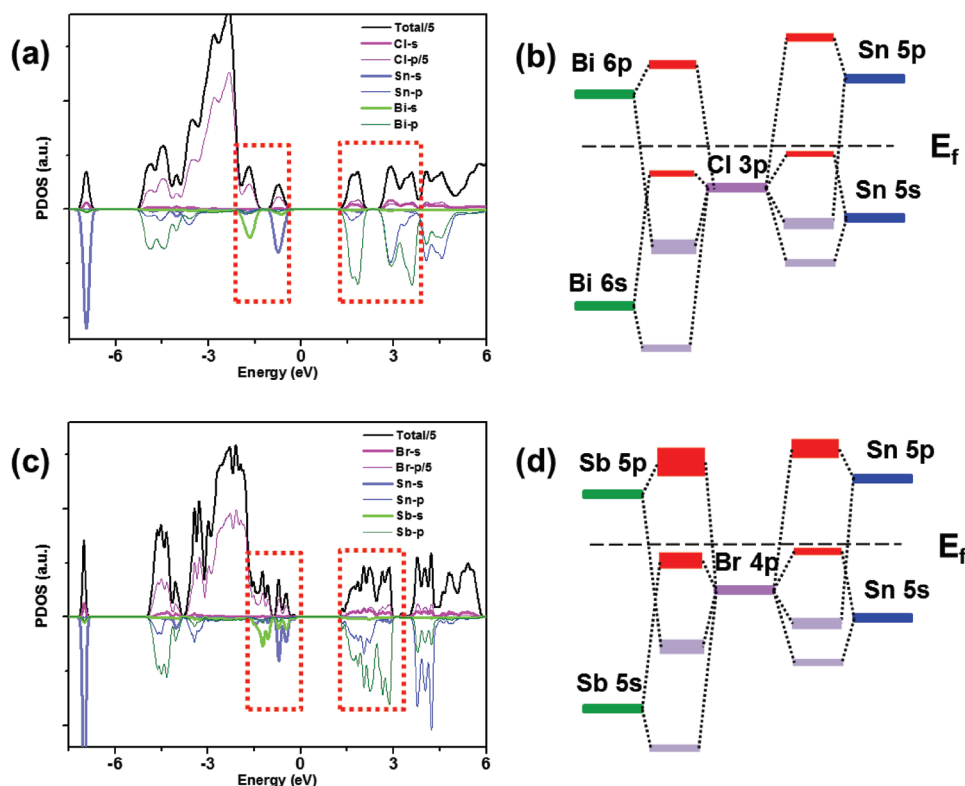


Figure 5. a,c) PBE+SOC calculated atomic orbital projected density of states (PDOS) for $K_4SnBi_2Cl_{12}$ and $Rb_4SnSb_2Br_{12}$, respectively. The discrete band edges contributed by different orbitals are highlighted by the red dashed rectangles. b,d) Schematically shown the orbital hybridization between metal cation and halide ion for the band edge states in $K_4SnBi_2Cl_{12}$ and $Rb_4SnSb_2Br_{12}$, respectively.

The layered $A_4MM'_2X_{12}$ perovskite is a B-site cation ordering structure which can be treated as a subgroup of the parent ABX_3 perovskites. Similar tilting modes can be used to enumerate the cation ordered layered structures, i.e., the M_3^+ and R_4^+ octahedral tilting mode in $A_4MM'_2X_{12}$ perovskites. However, it involves more complexity due to the layered charge ordering and its discontinuity along the [111] direction. In most cases, there exist tilting equivalents due to the cubic symmetry of the parent group, but the B-site cation order along the [111] direction makes the R_4^+ octahedral tilting to distinguishing between a positive ($a^-b^-c^0$) and a negative rotation ($-a^-b^-c^0$) along the [110] axis.^[34,35] The manifested octahedral tilting ($a^-b^-c^0$) in the relaxed Rb- and K-based $A_4MM'_2X_{12}$ perovskites begs further explaining of the physical origin of this tilting preference during the structure stabilization from the flat layered structures ($a^0b^0c^0$).

We illustrate the imposed electrostatic energy from the charge order coupling with the structure distortion by a simple model. As schematically shown in **Figure 7a**, the $\langle 111 \rangle$ -orientated tri-layered halide perovskite exhibits positive or negative net charges at each atomic plane, and the interfacial dipoles between them give rise to an internal electric field E .^[59,60] We employ a series of Gaussian surface between the polar atomic planes rising an alternative electric field profile ($-2, +1, -1, +1, -1, +2$) and finally become converged when across the 7 atomic planes due to the charge neutral of tri-layered perovskites. Thus, upon crossing the first negatively charged plane the potential gradient becomes negative (-2), and then become

reversed (+1) after crossing the second positively charged plane. Consequently, the electrostatic potential ϕ undergoes a dipole shift from the first atomic plane in combined with the symmetric oscillation component.^[60]

The octahedron tilting involves ion displacement from the flat atomic planes, thereby influencing electrostatic interactions from the charge redistribution.^[34,36] The R_4^+ octahedral tilting ($a^-b^-c^0$) has X^- ions departure from the $[AX_3]^{2-}$ planes to compensate the nearby M^{3+} positive charges thus reduces the interfacial dipole between the M^{3+} and M^{2+} atomic plane. As shown in the middle of **Figure 7b**, the $[M'X_6]^{3-}$ octahedrons are slightly reclining while the $[MX_6]^{4-}$ octahedron in the middle layer is erecting, which facilitates the X^- ions closer to the M^{3+} atomic planes and departure from the middle M^{2+} atomic planes. Likewise, when the $a^-b^-c^0$ tilting structures further invoked by M_3^+ tilting (see the $a^-b^-c^+$ tilting mode), the rotated X^- ion increases the amplitudes of intermixing and accompanies a lattices contraction along the rotation plane. To demonstrate the tilting preference coupling with the ordered charge planes, we have compared the homologous structure with equal negative octahedral rotation ($-a^-b^-c^0$) amplitude, as shown in **Figure S3** in the Supporting Information. Consequently, the opposite electrostatic interactions are expected due to the $[M'X_6]^{3-}$ octahedron undergoes erecting while the $[MX_6]^{4-}$ octahedron is reclining. The X^- ions are closer to the middle M^{2+} atomic planes and departure from the M^{3+} atomic planes, thus leading to an energetic penalty from the enhanced dipole between M^{2+} and $[AX_3]^{2-}$ atomic planes. To confirm our analysis, we have

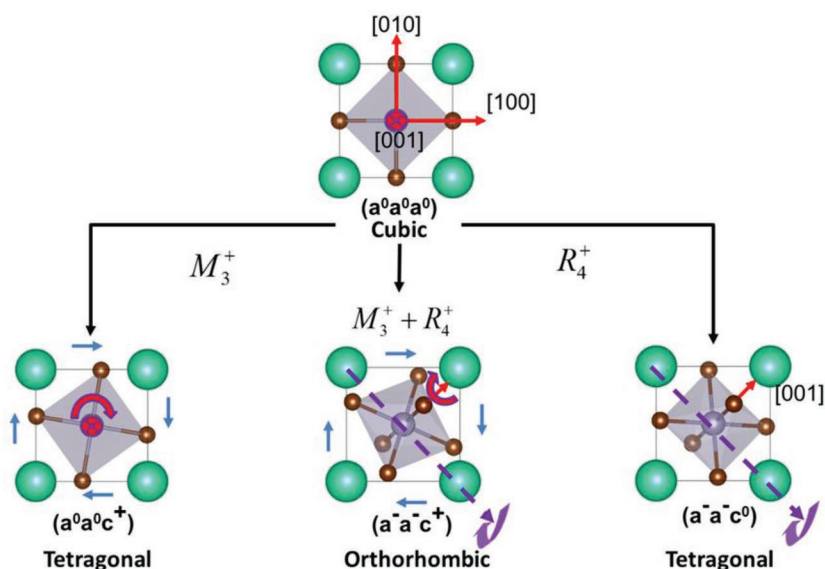


Figure 6. Structural models illustration for the typical Glazer notation in CsSnBr₃ halide perovskites under different tilting mode.

compared the relative energy in Rb₄SnSb₂Br₁₂ with different tilt modes, which shows consistent structural stability in the order of $-a^-b^-c^0 < a^0b^0c^0 < a^-b^-c^0 < a^-b^-c^+$.

Further evidence to support the above electrostatic analysis can be understood from the plane averaged electrostatic potential. As compared in Figure 7c, the intense oscillation of potential energy in the Rb₄SnSb₂Br₁₂ ($a^0b^0c^0$) become smoother in other three tilting structures due to the dipole reduction from the charged planes by ions intermixing. Particularly, in the $-a^-b^-c^0$ and $a^0b^0c^0$ tilting modes, the potential energy in the middle [RbBr₃]²⁻ atomic planes are lower than that on the surface. This is consistent with a higher electron density at the middle atomic planes (see the black and blue arrows in Figure S4 in the Supporting Information). For $a^0b^0c^0$ layered structures, a higher electron density on the middle planes can be inferred from the extra electron transfer from the Sn²⁺

layer. While in the $-a^-b^-c^0$ tilting mode, the Br⁻ ions are more close to the middle Sn²⁺ atomic plane yields a higher electron density in the middle layer, thereby further increasing the surface dipole shift.^[60] On the contrary, it suggests that the potential energy on the surface [RbBr₃]²⁻ layers are much lower than the middle layers in $a^-b^-c^0$ and $a^-b^-c^+$ tilting modes for the ions changing close to the Sb³⁺ atomic planes. The relieved surface dipole shift is in accordance with the charge compensation by the Br⁻ ions closer to the Sb³⁺ atomic planes.

3.4. Effects of Tilting on the Electronic Properties

Electronic properties of inorganic halide perovskites are closely correlated to the octahedral tilting due to the associated bonding angle changes.^[34,53] We here demonstrate that a certain cooperative structural distortion to the layered A₄MM'₂X₁₂ perovskites can systematically tune the electronic band structure including the bandgaps and band dispersions. For instance, the band structures of K₄SnSb₂Br₁₂ have changed remarkably in different tilt modes. As plotted in Figure 8a,b, the R₄⁺ tilting changing from $a^0b^0c^0$ to $a^-b^-c^0$ mode can stabilize the Sn(5s)-Br(4p) antibonding orbitals for valence band edges, but that destabilize the Sn(5p)-Br(4p)-Sb(5p) antibonding states in the conduction bands. Consequently, the bandgap increases and the band dispersion diminishes when bending of linear apical Sn-Br-Sb bonding away from its maximal antibonding overlapping.

Further, the $a^-b^-c^+$ tilting requires an additional out-of-plane component to bend the equator Sn-Br-Sb bond angles. This would lower the symmetry of the lattice even more and increase the Br(s/p) orbital hybridization, resulting in an enhanced antibonding between the equatorial

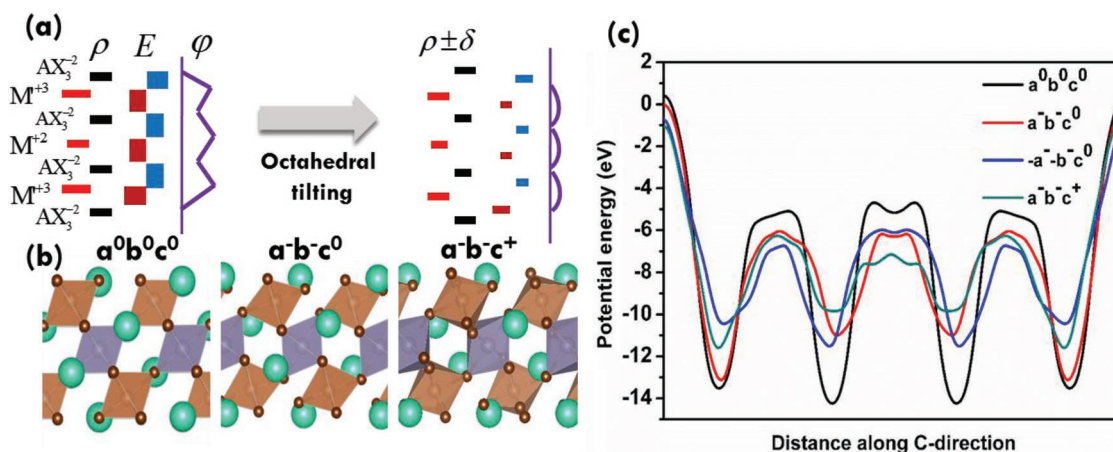


Figure 7. a) Schematics that depict the electrostatic energy reduction from the dipole compensation across the charged atomic plane in layered A₄MM'₂X₁₂ perovskites by octahedral tilting and their favorable tilting modes are shown in b). c) The comparison of plane averaged electrostatic potential for the Rb₄SnSb₂Br₁₂ in different tilt modes.

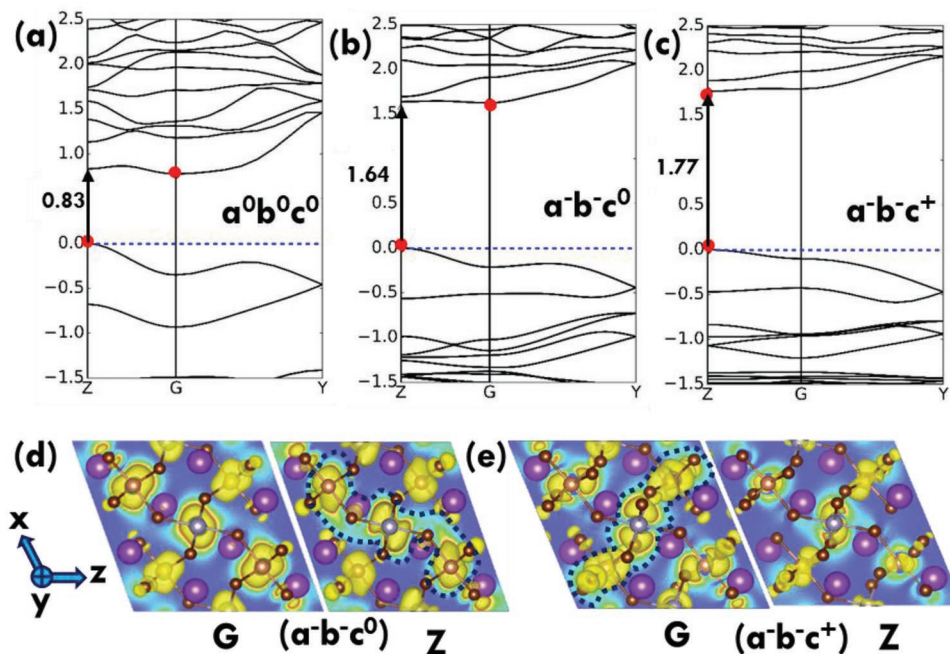


Figure 8. a–c) PBE+SOC calculated band structures for the $K_4\text{SnSb}_2\text{Br}_{12}$ in different tilt modes. d,e) Represent the conduction band edge charge density contours (with isosurface of 2.5×10^{-4}) at G (left) and Z (right) points for b) $a^-b^-c^0$ and c) $a^-b^-c^+$ tilting mode, respectively. The blue dashed regions highlight the intense antibonding orbital interactions.

Sb(p)-Br(s/p) hybrid orbitals. Interestingly, the increased equatorial bonding intrigues the indirect-to-direct band transition due to the more upshift conduction band edge at G than Z point, see in Figure 8c. Note that the perovskites with indirect bandgap features are known to be beneficial for carrier recombination rates in optical absorbers, while the direct bandgaps would be a good attribute for light emission applications.^[2,61–63] Considering the strong direct gap optical transition and their bandgaps are in the visible light range (2.1–2.7 eV), the perovskites promise for high sensitivity detectors and efficient light-emitting diodes (LEDs) applications.^[64–66] The semiconductor detectors with large energy gaps (1.6–3.0 eV) can reduce the dark current noise from thermally activated carrier hopping.^[55] Additionally, the 2D layered structure in these perovskites provides a spatial limitation on the diffusion length of excitons and reduces the possibility of exciton dissociation into free carriers, and are, therefore, thought to be suitable for application as the light emissive layer in LEDs.^[64] These tilting modes couple with the electronic bands to give a versatile approach to tune the optoelectronic properties of the layered perovskites. To show the subtle variation, we plot the conduction band electron charge density contours at G (left) and Z (right) points under different tilting mode. As the electron charge density contour is shown in Figure 8d,e, the $a^-b^-c^0$ tilting mode exhibits more intense Sn(5p)-Br(4p)-Sb(5p) antibonding repulsion along the apical direction at Z point due to the in-plane bending of linear apical Sn–Br–Sb bonds. However, the $a^-b^-c^+$ tilting mode significantly diminishes the apical Sn–Br–Sb orbital interactions but intensify antibonding between the equatorial Sb(p)-Br(s/p)-Sn(p) hybrid orbitals extending in the γ -direction at G point.

4. Conclusion

We take mixed cations of M^{2+} (Zn^{2+} and Sn^{2+}) plus M'^{3+} (Bi^{3+} and Sb^{3+}) to explore the novel $\langle 111 \rangle$ -oriented tri-layered halide perovskites by computational screening the possible ion combinations in the target $A_4MM'_2X_{12}$. We have determined the lowest ground state with (C2/m) scaffolds and cation ordered atomic configurations, then take two filters to determine the thermodynamic stability of the compounds. After the thermodynamic filters, 6 stable compounds were obtained, i.e., $K_4\text{SnBi}_2\text{Cl}_{12}$, $K_4\text{SnSb}_2\text{Cl}_{12}$, $K_4\text{SnSb}_2\text{Br}_{12}$, $\text{Rb}_4\text{SnBi}_2\text{Cl}_{12}$, $\text{Rb}_4\text{SnSb}_2\text{Br}_{12}$, and $\text{Rb}_4\text{SnSb}_2\text{Cl}_{12}$. These 6 compounds have indirect band transition (2.1–2.7 eV) from G to Z point. The energy difference between direct and indirect bandgaps in these compounds is very small (0.02–0.12 eV). Additionally, it clearly shows the chemical trend that the bandgap values increase with changing the large ionic radius to smaller ones for $A_4\text{SnM}'_2\text{X}_{12}$. This is because the smaller K^+ cation induces larger bond angle distortions in the $[\text{SnX}_6]^{4-}$ octahedrons, which destabilizes the antibonding from X(s/p) hybridization with the Sn(5p) orbitals while stabilizes it with the Sn(5s) orbitals, thus elevating the CBM and reducing the VBM. We further identify the physical origin of tilting preference in the layered Rb- and K-based $A_4MM'_2X_{12}$ compounds by an electrostatic model. These tilting modes correlate to the electronic bands and give a versatile approach to tune the electronic properties of the layered perovskites, such as the increased bandgaps and indirect-to-direct bandgap transitions. Apart from the inorganic cation mixing, it is intuitively to envision hybrid bulky cations as methylammonium or formamidinium in the A site of $A_4MM'_2X_{12}$ to stabilize the iodine-based perovskites. Though it might be difficult to direct synthesis the $\langle 111 \rangle$ -orientated layered hybrid perovskites with

single organic cation occupied on the A-site due to the large tolerance factors.^[67] Nevertheless, it is still possible to stabilize the mixed organic–inorganic cations by entropy or structural compensation for postsynthesis modification of perovskites as the partial experimental evidence of these compositions.^[13] Thus we are confident in these new mixed-cation perovskites to be synthesized by the developing technics such as sequential deposition, cation intercalation, or exchange reaction.

Supporting Information

Supporting Information is available from the Wiley Online Library or from the author.

Acknowledgements

Work at Jilin University is supported by the National Natural Science Foundation of China (Grant No. 61722403 and 11674121), the National Key Research and Development Program of China (Grant No. 2016YFB0201204), and Program for Jilin University Science and Technology Innovative Research Team. Calculations were performed in part at High Performance Computing Center of Jilin University.

Conflict of Interest

The authors declare no conflict of interest.

Keywords

halide perovskites, lead-free, materials by design, optoelectronic applications

Received: March 3, 2019
Revised: April 4, 2019
Published online: May 6, 2019

- [1] B. Saparov, D. B. Mitzi, *Chem. Rev.* **2016**, *116*, 4558.
- [2] W.-J. Yin, T. Shi, Y. Yan, *J. Phys. Chem. C* **2015**, *119*, 5253.
- [3] J. Even, L. Pedesseau, C. Katan, M. Kepenekian, J.-S. Lauret, D. Sapori, E. Deleporte, *J. Phys. Chem. C* **2015**, *119*, 10161.
- [4] J. Cui, H. Yuan, J. Li, X. Xu, Y. Shen, H. Lin, M. Wang, *Sci. Technol. Adv. Mater.* **2015**, *16*, 036004.
- [5] Z. Xiao, Y. Yan, *Adv. Energy Mater.* **2017**, *7*, 1701136.
- [6] Q. Jiang, Y. Zhao, X. Zhang, X. Yang, Y. Chen, Z. Chu, Q. Ye, X. Li, Z. Yin, J. You, *Nat. Photonics* **2019**, <https://doi.org/10.1038/s41566-019-0398-2>.
- [7] R. E. Brandt, V. Stevanović, D. S. Ginley, T. Buonassisi, *MRS Commun.* **2015**, *5*, 265.
- [8] W.-J. Yin, J.-H. Yang, J. Kang, Y. Yan, S.-H. Wei, *J. Mater. Chem. A* **2015**, *3*, 8926.
- [9] X. Qin, Z. Zhao, Y. Wang, J. Wu, Q. Jiang, J. You, *J. Semicond.* **2017**, *38*, 011002.
- [10] X. He, D. J. Singh, P. Boon-on, M.-W. Lee, L. Zhang, *J. Am. Chem. Soc.* **2018**, *140*, 18058.
- [11] F. Hao, C. C. Stoumpos, D. H. Cao, R. P. H. Chang, M. G. Kanatzidis, *Nat. Photonics* **2014**, *8*, 489.
- [12] Y. Li, W. Sun, W. Yan, S. Ye, H. Rao, H. Peng, Z. Zhao, Z. Bian, Z. Liu, H. Zhou, C. Huang, *Adv. Energy Mater.* **2016**, *6*, 1601353.
- [13] F. Xu, T. Zhang, G. Li, Y. Zhao, *J. Mater. Chem. A* **2017**, *5*, 11450.
- [14] N. Li, Z. Zhu, C.-C. Chueh, H. Liu, B. Peng, A. Petrone, X. Li, L. Wang, A. K.-Y. Jen, *Adv. Energy Mater.* **2017**, *7*, 1601307.
- [15] Y. Liao, H. Liu, W. Zhou, D. Yang, Y. Shang, Z. Shi, B. Li, X. Jiang, L. Zhang, L. N. Quan, R. Quintero-Bermudez, B. R. Sutherland, Q. Mi, E. H. Sargent, Z. Ning, *J. Am. Chem. Soc.* **2017**, *39*, 6693.
- [16] H. Tsai, W. Nie, J.-C. Blancon, C. C. Stoumpos, R. Asadpour, B. Harutyunyan, A. J. Neukirch, R. Verduzco, J. J. Crochet, S. Tretiak, L. Pedesseau, J. Even, M. A. Alam, G. Gupta, J. Lou, P. M. Ajayan, M. J. Bedzyk, M. G. Kanatzidis, A. D. Mohite, *Nature* **2016**, *536*, 312.
- [17] A. J. Lehner, D. H. Fabini, H. A. Evans, C.-A. Hébert, S. R. Smock, J. Hu, H. Wang, J. W. Zwanziger, M. L. Chabiny, R. Seshadri, *Chem. Mater.* **2015**, *27*, 7137.
- [18] P. C. Harikesh, H. K. Mulmudi, B. Ghosh, T. W. Goh, Y. T. Teng, K. Thirumal, M. Lockrey, K. Weber, T. M. Koh, S. Li, S. Mhaisalkar, N. Mathews, *Chem. Mater.* **2016**, *28*, 7496.
- [19] Q. Xu, D. Yang, J. Lv, Y.-Y. Sun, L. Zhang, *Small Methods* **2018**, *2*, 1700316.
- [20] X.-G. Zhao, J.-H. Yang, Y. Fu, D. Yang, Q. Xu, L. Yu, S.-H. Wei, L. Zhang, *J. Am. Chem. Soc.* **2017**, *139*, 2630.
- [21] M. R. Filip, S. Hillman, A. A. Haghghirad, H. J. Snaith, F. Giustino, *J. Phys. Chem. Lett.* **2016**, *7*, 2579.
- [22] X.-G. Zhao, D. Yang, J.-C. Ren, Y. Sun, Z. Xiao, L. Zhang, *Joule* **2018**, *2*, 1662.
- [23] X.-G. Zhao, D. Yang, Y. Sun, T. Li, L. Zhang, L. Yu, A. Zunger, *J. Am. Chem. Soc.* **2017**, *139*, 6718.
- [24] F. Igbari, Z.-K. Wang, L.-S. Liao, *Adv. Energy Mater.* **2019**, *9*, 1803150.
- [25] W. Meng, X. Wang, Z. Xiao, J. Wang, D. B. Mitzi, Y. Yan, *J. Phys. Chem. Lett.* **2017**, *8*, 2999.
- [26] B. Saparov, F. Hong, J.-P. Sun, H.-S. Duan, W. Meng, S. Cameron, I. G. Hill, Y. Yan, D. B. Mitzi, *Chem. Mater.* **2015**, *27*, 5622.
- [27] F. Jiang, D. Yang, Y. Jiang, T. Liu, X. Zhao, Y. Ming, B. Luo, F. Qin, J. Fan, H. Han, L. Zhang, Y. Zhou, *J. Am. Chem. Soc.* **2018**, *140*, 1019.
- [28] P. Gratia, I. Zimmermann, P. Schouwink, J.-H. Yum, J.-N. Audinot, K. Sivula, T. Wirtz, M. K. Nazeeruddin, *ACS Energy Lett.* **2017**, *2*, 2686.
- [29] G. Tang, Z. Xiao, H. Hosono, T. Kamiya, D. Fang, J. Hong, *J. Phys. Chem. Lett.* **2018**, *9*, 43.
- [30] B. Vargas, E. Ramos, E. Pérez-Gutiérrez, J. C. Alonso, D. Solís-Ibarra, *J. Am. Chem. Soc.* **2017**, *139*, 9116.
- [31] B. Vargas, R. Torres-Cadena, J. Rodríguez-Hernández, M. Gembicky, H. Xie, J. Jiménez-Mier, Y.-S. Liu, E. Menéndez-Proupin, K. R. Dunbar, N. Lopez, P. Olalde-Velasco, D. Solís-Ibarra, *Chem. Mater.* **2018**, *30*, 5315.
- [32] J. Xu, J.-B. Liu, J. Wang, B.-X. Liu, B. Huang, *Adv. Funct. Mater.* **2018**, *28*, 1800332.
- [33] F. Brivio, J. M. Frost, J. M. Skelton, A. J. Jackson, O. J. Weber, M. T. Weller, A. R. Goñi, A. M. A. Leguy, P. R. F. Barnes, A. Walsh, *Phys. Rev. B* **2015**, *92*, 144308.
- [34] J. Young, J. M. Rondinelli, *J. Phys. Chem. Lett.* **2016**, *7*, 918.
- [35] C. J. Howard, H. T. Stokes, *Acta Crystallogr., Sect. B: Struct. Sci.* **2004**, *60*, 674.
- [36] R. X. Yang, J. M. Skelton, E. L. da Silva, J. M. Frost, A. Walsh, *J. Phys. Chem. Lett.* **2017**, *8*, 4720.
- [37] S. Boyer-Richard, C. Katan, B. Traoré, R. Scholz, J.-M. Jancu, J. Even, *J. Phys. Chem. Lett.* **2016**, *7*, 3833.
- [38] T. Zhu, G. Khalsa, D. M. Hvas, A. S. Gibbs, W. Zhang, P. S. Halasyamani, N. A. Benedek, M. A. Hayward, *Chem. Mater.* **2018**, *30*, 8915.
- [39] P. E. Blöchl, *Phys. Rev. B* **1994**, *50*, 17953.

- [40] G. Kresse, D. Joubert, *Phys. Rev. B* **1999**, *59*, 1758.
- [41] J. Klimeš, D. R. Bowler, A. Michaelides, *J. Phys.: Condens. Matter* **2010**, *22*, 022201.
- [42] J. P. Perdew, K. Burke, M. Ernzerhof, *Phys. Rev. Lett.* **1996**, *77*, 3865.
- [43] J. Heyd, G. E. Scuseria, M. Ernzerhof, *J. Chem. Phys.* **2003**, *118*, 8207.
- [44] G. K. H. Madsen, D. J. Singh, *Comput. Phys. Commun.* **2006**, *175*, 67.
- [45] D. Yang, J. Lv, X. Zhao, Q. Xu, Y. Fu, Y. Zhan, A. Zunger, L. Zhang, *Chem. Mater.* **2017**, *29*, 524.
- [46] R. Fischer, B. G. Müller, *Z. Anorg. Allg. Chem.* **2002**, *628*, 1532.
- [47] S. W. Kim, R. Zhang, P. S. Halasyamani, M. A. Hayward, *Inorg. Chem.* **2015**, *54*, 6647.
- [48] M. H. Du, *J. Mater. Chem. C* **2014**, *2*, 4784.
- [49] Y. G. Yu, X. Zhang, A. Zunger, *Phys. Rev. B* **2017**, *95*, 085201.
- [50] R. Gautier, X. Zhang, L. Hu, L. Yu, Y. Lin, T. O. L. Sunde, D. Chon, K. R. Poepplmeier, A. Zunger, *Nat. Chem.* **2015**, *7*, 308.
- [51] J. P. Perdew, A. Zunger, *Phys. Rev. B* **1981**, *23*, 5048.
- [52] L. Pedesseau, J.-M. Jancu, A. Rolland, E. Deleporte, C. Katan, J. Even, *Opt. Quantum Electron.* **2014**, *46*, 1225.
- [53] J. L. Knutson, J. D. Martin, D. B. Mitzi, *Inorg. Chem.* **2005**, *44*, 4699.
- [54] M. I. Dar, G. Jacopin, S. Meloni, A. Mattoni, N. Arora, A. Boziki, S. M. Zakeeruddin, U. Rothlisberger, M. Grätzel, *Sci. Adv.* **2016**, *2*, e1601156.
- [55] C. C. Stoumpos, C. D. Malliakas, J. A. Peters, Z. Liu, M. Sebastian, J. Im, T. C. Chasapis, A. C. Wibowo, D. Y. Chung, A. J. Freeman, B. W. Wessels, M. G. Kanatzidis, *Cryst. Growth Des.* **2013**, *13*, 2722.
- [56] T. M. Brenner, D. A. Egger, L. Kronik, G. Hodes, D. Cahen, *Nat. Rev. Mater.* **2016**, *1*, 15007.
- [57] L. Yu, R. S. Kokenyesi, D. A. Keszler, A. Zunger, *Adv. Energy Mater.* **2013**, *3*, 43.
- [58] M. T. Greiner, T. E. Jones, S. Beeg, L. Zwiener, M. Scherzer, F. Girgsdies, S. Piccinin, M. Armbrüster, A. Knop-Gericke, R. Schlögl, *Nat. Chem.* **2018**, *10*, 1008.
- [59] P. V. Balachandran, J. M. Rondinelli, *Nat. Commun.* **2015**, *6*, 6191.
- [60] W. A. Harrison, E. A. Kraut, J. R. Waldrop, R. W. Grant, *Phys. Rev. B* **1978**, *18*, 4402.
- [61] T. Kirchartz, U. Rau, *J. Phys. Chem. Lett.* **2017**, *8*, 1265.
- [62] P. Azarhoosh, S. McKechnie, J. M. Frost, A. Walsh, M. van Schilfgaarde, *APL Mater.* **2016**, *4*, 091501.
- [63] T. Wang, B. Daiber, J. M. Frost, S. A. Mann, E. C. Garnett, A. Walsh, B. Ehrler, *Energy Environ. Sci.* **2017**, *10*, 509.
- [64] C. Bao, J. Yang, S. Bai, W. Xu, Z. Yan, Q. Xu, J. Liu, W. Zhang, F. Gao, *Adv. Mater.* **2018**, *30*, 1803422.
- [65] Q. V. Le, M. Park, W. Sohn, H. W. Jang, S. Y. Kim, *Adv. Electron. Mater.* **2017**, *3*, 1600448.
- [66] M. Long, P. Wang, H. Fang, W. Hu, *Adv. Funct. Mater.* **2018**, *1803807*.
- [67] K. Eckhardt, V. Bon, J. Getzschmann, J. Grothe, F. M. Wisser, S. Kaskel, *Chem. Commun.* **2016**, *52*, 3058.